PAPER

Orbital competition of Mn^{3+} and V^{3+} ions in Mn$_{1+x}$V$_{2-x}$O$_4$

View the article online for updates and enhancements.

Orbital competition of Mn^{3+} and V^{3+} ions in $Mn_{1+x}V_{2-x}O_4$

J L Jiao[1] , **H P Zhang**[2], **Q Huang**[3], **W Wang**[1], **R Sinclair**[3], **G Wang**[1], **Q Ren**[1], **G T Lin**[1], **A Huq**[4], **H D Zhou**[3], **M Z Li**[2] and **J Ma**[1,*]

[1] Key Laboratory of Artificial Structures and Quantum Control (Ministry of Education), Shenyang National Laboratory for Materials Science, School of Physics and Astronomy, Shanghai Jiao Tong University, Shanghai 200240, People's Republic of China
[2] Department of Physics, Beijing Key Laboratory of Opto-electronic Functional Materials & Micro-nano Devices, Renmin University of China, Beijing 100872, People's Republic of China
[3] Department of Physics and Astronomy, University of Tennessee, Knoxville, Tennessee 37996, United States of America
[4] Neutron Scattering Division, Oak Ridge National Laboratory, Oak Ridge, Tennessee 37381, United States of America

E-mail: jma3@sjtu.edu.cn

CrossMark

Abstract

The structural and magnetic properties of $Mn_{1+x}V_{2-x}O_4$ ($0 < x \leqslant 1$) have been investigated by the heat capacity, magnetization, x-ray diffraction and neutron diffraction measurements, and a phase diagram of temperature versus composition was built up. For $x \leqslant 0.3$, a cubic-to-tetragonal ($c > a$) phase transition was observed. For $x > 0.3$, the system maintained the tetragonal lattice. Although the collinear and noncollinear magnetic transitions of V^{3+} ions were obtained in all compositions, the canting angles between the V^{3+} ions decreased with Mn^{3+}-doping, and the ordering of the Mn^{3+} ions was only observed as $x > 0.4$. In order to study the dynamics of the ground state, the first principles simulation was applied to analyze not only the orbital effects of Mn^{2+}, Mn^{3+}, and V^{3+} ions, but also the related exchange energies.

(Some figures may appear in colour only in the online journal)

1. Introduction

Currently, frustrated magnets have attracted a lot of attention in both scientific and industrial fields due to their degenerate ground state which gives rise to a host of exotic phenomena such as spin ices and spin liquids [1–3]. Since the degeneracy of the ground state could be affected by the external stimuli such as magnetic or electric fields, pressure, and temperature, the exotic physical properties could be harnessed if one could understand the original driving force of the frustrated state. Typically, the geometrically frustrated lattice includes the corner- and side-shared triangle as the two-dimensional (2D) kagome and triangular compounds, and the three-dimensional (3D) spinel and pyrochlore compounds [2, 4, 5]. Spinel oxides, AB_2O_4, are naturally geometrically frustrated materials on the pyrochlore sublattice at the B-sites. For these compounds, the spin, orbital, charge and lattice degrees of freedom are strongly correlated and compete with each other to induce varieties of ordered states which influence the macroscopic properties of the system, such as the structural, electric, and magnetic properties [6–10]. As a result, interesting physical properties have been observed in spinel oxides, such as the colossal magnetoresistance effect, the giant magnetoelectric effect, and multiferroicity [11, 12]. If the electrons don't fill up the energy

levels, the degenerate orbitals could be interfered with the crystal field, and the lattice will be distorted by the Jahn–Teller (JT) effect [13]. Moreover, the orbital could even couple the spin to relieve the magnetic frustration, resulting in a magnetically ordered state [14].

Vanadate spinel, AV_2O_4, has the magnetic V^{3+} ($3d^2$, $S = 1$) ions at the B-site, and is an ideal system to study the complex interplay of electron, spin, lattice and orbit. The octahedral crystal field accompanied by $6O^{2-}$ ions around the central V^{3+} ion can split the $3d$ orbitals of the V^{3+} ion into t_{2g} orbitals with lower energy and e_g orbitals with higher energy. Due to the JT effect, the degeneracy of the t_{2g} orbitals will be further released, and two electrons of the V^{3+} ion will choose single orbitals with the lowest energy spontaneously. Several theoretical models have been proposed to clarify such orbital ordering of the V^{3+} ion [15–17].

In MnV_2O_4, the V^{3+} ions are influenced under the internal magnetic field from the A-site Mn^{2+} ions, which makes MnV_2O_4 exhibit several phase transitions: paramagnetism (PM)-to-collinear ferrimagnetism (CF) and collinear-to-noncollinear ferrimagnetism (NCF) along with a structural phase transition from a cubic to a tetragonal lattice ($c < a$) [18, 19]. Since the magnetic and structural phase transitions happen at the same temperature, there is a debate on the driving force of the ferrimagnetic order and the tetragonal structural transition. Based on previous work [19], the orbital effect of V^{3+} ion was believed to relate both the magnetic and structural transitions. However, Ma *et al* [20] found that the CF–NCF transition was decoupled from the cubic-tetragonal structural phase transition with substituted Mn^{2+} ions by Co^{2+} ions on A-sites as $Mn_{1-x}Co_xV_2O_4$, and the orbital ordering of the V^{3+} ion completely disappeared while the NCF phase still existed. These manifested the independence between Yafet–Kittel (YK) magnetic transition and structural phase transition. Although the Co^{2+} ions only introduced an internal magnetic field the same as Mn^{2+} ions, the itineracy increased in the system, and the localized orbital ordering of the V^{3+} ions was influenced. In order to investigate the exact orbital effect of the V^{3+} ions, it is essential to gradually substitute the V^{3+} ions with a nonmagnetic ion or one with different magnetic/orbital properties. The Mn^{3+} ($3d^4$, $S = 2$) ion has an orbital effect on e_g orbitals, ($3z^2–r^2$), which is extended in the basal *ab*-plane in an octahedral environment as the tetragonal phase ($c > a$) in Mn_3O_4 [21–23]. Hence, doping Mn^{3+} ions on the V^{3+}-site provided a perfect example to study the orbital properties of the V^{3+} ions. In this work, we modulated constituents of B-site ions and studied the structural and magnetic properties of $Mn_{1+x}V_{2-x}O_4$ ($0 < x \leqslant 1$) by magnetization, heat capacity, x-ray powder diffraction x-ray diffraction (XRD) and neutron powder diffraction (NPD) measurements as well as the first principle simulation. Our results confirmed the phase splitting between the crystal structure and magnetic structure. The magnetic transition still existed while the crystal structure maintained tetragonal phase ($c > a$) in the whole temperature range for high doping ($x \geqslant 0.4$). The transition temperature decreased with increasing x, which implied the strong competition between exchange interactions J_{AB} and J_{BB}. Two other

noncollinear phase transitions related to V^{3+} and Mn^{3+} ions were also determined.

2. Sample synthesis and experiments

Polycrystalline samples of $Mn_{1+x}V_{2-x}O_4$ ($0 < x \leqslant 1$) were synthesized by solid state reaction. Stoichiometric mixtures of MnO, V_2O_3, and V_2O_5 were ground together and calcined under flowing Ar in a sealed quartz tube at 900 °C for 100 h. A quantum design physical property measurements system was applied to measure the magnetization with a field of $H = 100$ Oe and the specific heat from 2 K to 300 K. The XRD patterns were recorded by an HUBER imaging-plate Guinier camera 670 with Ge monochromatized Cu $K_{\alpha1}$ radiation from 10 K to 300 K with a cryogenic helium compressor unit. NPD measurements were performed at the POWGEN diffractometer [24] at the spallation neutron source, and the NPD (HB-2A) at the high flux isotope reactor (HFIR), oak ridge national laboratory (ORNL). Approximately 1.5 g of powdered $Mn_{1+x}V_{2-x}O_4$ ($x = 0.1$, 0.2, and 0.3) were loaded into Vanadium cans in the sample changer at POWGEN, and the patterns were collected from 10 K to 90 K. Approximately 3 g of powdered $Mn_{1+x}V_{2-x}O_4$ ($x = 0.1$, 0.2, and 0.3) were measured at HB-2A at temperatures of 1.5 K and 150 K using both 1.54 Å and 2.41 Å wavelengths, and the collimation was set as open-21'-12'. The shorter wavelength was used to investigate the crystal structures, while the longer wavelength provided lower Q coverage with better resolution that was important for investigating the magnetic structures of the material. The diffraction data were analyzed by the refinement program FullProf [25].

3. Results

3.1. XRD and NPD

The composition- and temperature-dependence of XRD powder diffraction were measured from 10 K to 300 K and analyzed by the Rietveld refinement with the FULLPROF program [25]. Figures 1(a) and 1(b) presented the data and refinement of $Mn_{1+x}V_{2-x}O_4$ ($x = 0.3$ and 0.4) at 30 K and 300 K, respectively, and the refinement parameters of space group, lattice constants, and atomic positions were included in table 1. Similar as MnV_2O_4, the structure transition from cubic *Fd-3m* to tetragonal *I4₁/amd* symmetry was observed for $Mn_{1.3}V_{1.7}O_4$, however, the lattice constant ratios were different: $c/a < 1$ for MnV_2O_4 and $c/a > 1$ for $Mn_{1.3}V_{1.7}O_4$ as Mn_3O_4, which clearly demonstrated the orbital order competition between the Mn^{3+} ions and the V^{3+} ions [26, 27]. Moreover, there was no lattice transition from 10 K to 300 K for $x > 0.3$.

The temperature-dependence of (440) and (400) reflections were compared in figures 1(c) and (d), respectively. The full width at half maximum (FWHM) of both diffractions increased at T_S around 54 K with error bars for $Mn_{1.1}V_{1.9}O_4$, and a structural transition was suggested which was consistent with the heat capacity measurement. Meanwhile,

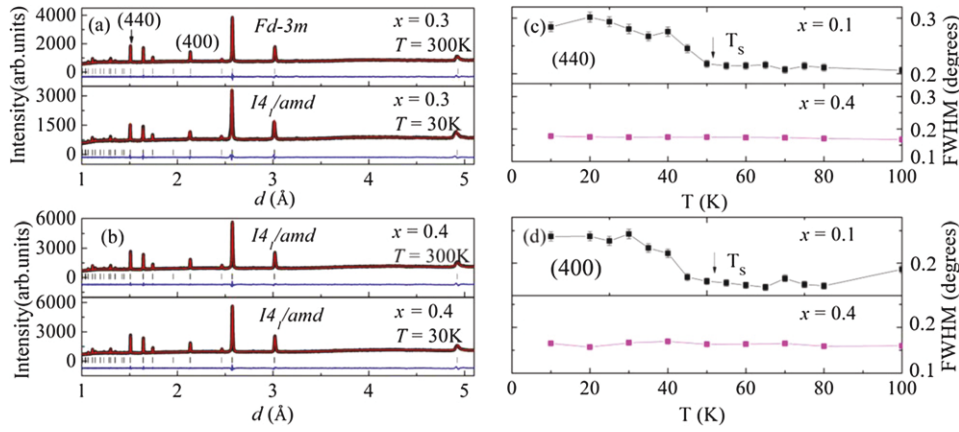**Figure 1.** XRD data of $Mn_{1+x}V_{2-x}O_4$ ($x = 0.1$, 0.3, and 0.4). Rietveld refinements of $Mn_{1.3}V_{1.7}O_4$ (a) and $Mn_{1.4}V_{1.6}O_4$ (b) by FULLPROF at 300 K and 30 K, respectively. The crystal structures of $Mn_{1.3}V_{1.7}O_4$ are cubic at 300 K and tetragonal at 30 K, while $Mn_{1.4}V_{1.6}O_4$ retains tetragonal symmetry at both temperatures. The temperature dependence of the FWHM of (440) (c) and (400) (d) diffractions for $Mn_{1.1}V_{1.9}O_4$ and $Mn_{1.4}V_{1.6}O_4$, respectively.

Table 1. XRD measurements on structural parameters for the $x = 0.3$ at 300 K (Fd-$3m$) and 30 K ($I4_1/amd$), and $x = 0.4$ at 300 K ($I4_1/amd$) and 30 K ($I4_1/amd$), respectively.

	Atom	Site	x	y	Z
$x = 0.3$, $T = 300K$					
Fd-$3m$	Mn (1)	8a	0.125	0.125	0.125
$a = 8.551$ Å	V	16d	0.5	0.5	0.5
$b = 8.551$ Å	Mn (2)	16d	0.5	0.5	0.5
$c = 8.551$ Å	O	32e	0.740	0.740	0.740
$\chi^2 = 2.34$, Rwp = 1.76%					
$x = 0.3$, $T = 30K$					
$I4_1/amd$	Mn (1)	4a	0.5	0.25	0.125
$a = 6.033$ Å	V	8c	0.25	0.75	0.25
$b = 6.033$ Å	Mn (2)	8c	0.25	0.75	0.25
$c = 8.549$ Å	O	32e	0.5	0.975	0.266
$\chi^2 = 1.93$, Rwp = 2.05%					
$x = 0.4$, $T = 300K$					
$I4_1/amd$	Mn (1)	4a	0.5	0.25	0.125
$a = 6.035$ Å	V	8c	0.25	0.75	0.25
$b = 6.035$ Å	Mn (2)	8c	0.25	0.75	0.25
$c = 8.549$ Å	O	32e	0.5	0.996	0.275
$\chi^2 = 1.16$, Rwp = 2.15%					
$x = 0.4$, $T = 30K$					
$I4_1/amd$	Mn (1)	4a	0.5	0.25	0.125
$a = 6.033$ Å	V	8c	0.25	0.75	0.25
$b = 6.033$ Å	Mn (2)	8c	0.25	0.75	0.25
$c = 8.545$ Å	O	32e	0.5	0.984	0.267
$\chi^2 = 2.11$, Rwp = 2.29%					

the FWHM of $Mn_{1.4}V_{1.6}O_4$ remained constant in the entire temperature range, and indicated no structural transition, figure 1(b) and table 1.

In order to investigate the lattice and magnetic structure, the NPDs were measured at POWGEN and HB-2A, ORNL. Figure 2 illustrated the (220) and (111) reflections

of $Mn_{1.2}V_{1.8}O_4$ at different temperatures, and both structural and magnetic signals were included. The peak broadening indicated a lattice distortion upon cooling down, while the increased intensities at ~60 K revealed the magnetic ordering. As for $Mn_{1+x}Co_xV_2O_4$ [10, 19], a magnetic transition from PM to CF and a structural transition from a cubic to a tetragonal lattice were observed at the same temperature. In order to examine the phase transitions more clearly, the temperature-dependence of intensities was plotted in figures 2(c), (d) and (g), (h). The related magnetic peak was analyzed by a power law [equation (1)] to study the critical behavior of the magnetic sublattice in $Mn_{1.2}V_{1.8}O_4$, figure 2(d),

$$ I = I_0 \left(1 - \frac{T}{T_N} \right)^{2\beta}, \tag{1} $$

where T_N is the Néel temperature, I_0 is the integrated intensity at base temperature, and β is the order parameter critical exponent. The obtained β is 0.35 for $Mn_{1.2}V_{1.8}O_4$, which is close to β_2 (0.34) of MnV_2O_4 [19] and the 3D Heisenberg ($\beta = 0.36$) model.

As shown in figure 3, the high resolution NPD measurements on $Mn_{1+x}V_{2-x}O_4$ ($x = 0.1$, 0.2, 0.3) were performed at 1.5 K and 150 K with $\lambda = 1.5401$ Å. Comparing the data at 150 K, the intensities of (111) reflections for $x = 0.1$, 0.2 and 0.3 increased at 1.5 K. For $x = 0.1$, the (400) reflection at 150 K clearly splits into two peaks at 1.5 K, and a structural phase transition of cubic-to-tetragonal phase has been confirmed. For $x = 0.2$ and 0.3, figures 3(e) and (f), although the diffraction splitting is not observed, the (400) reflections at 1.5 K are broader than at 150 K and the structural transition still exists. Moreover, the FWHM difference between 1.5 K and 150 K decreases from $x = 0.2$ to $x = 0.3$, which agrees with the XRD diffraction. Hence, the Mn-doping weakens the cubic-to-tetragonal lattice transition.

In figures 4(a) and (b), $Mn_{1.2}V_{1.8}O_4$ exhibited a cubic structural phase with PM at 90 K, which was compatible with the XRD measurements. As the temperature decreased, a tetragonal ($c > a$) structure with the spins of Mn^{2+} and V^{3+} aligning
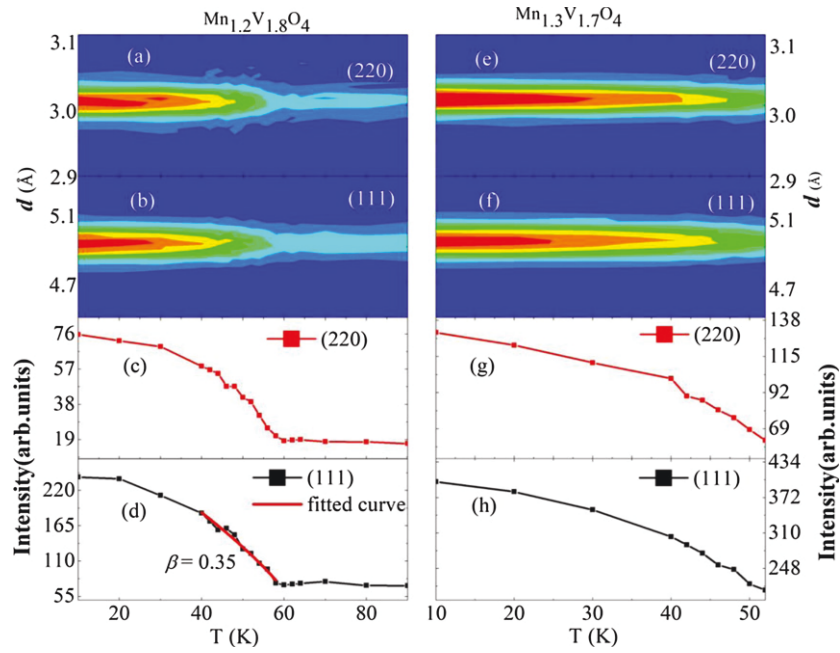
Figure 2. The temperature-dependence of the (220) and (111) Bragg peaks of $Mn_{1+x}V_{2-x}O_4$ for $x = 0.2$ [(a), (b)] and $x = 0.3$ [(e), (f)] by the NPD POWGEN, respectively. (c) and (d), (g) and -(h) are the related (220) and (111) peak intensities for $x = 0.2$ [(c), (d)] and $x = 0.3$ [(g), (h)]. The red line in (d) is fitted from power law.
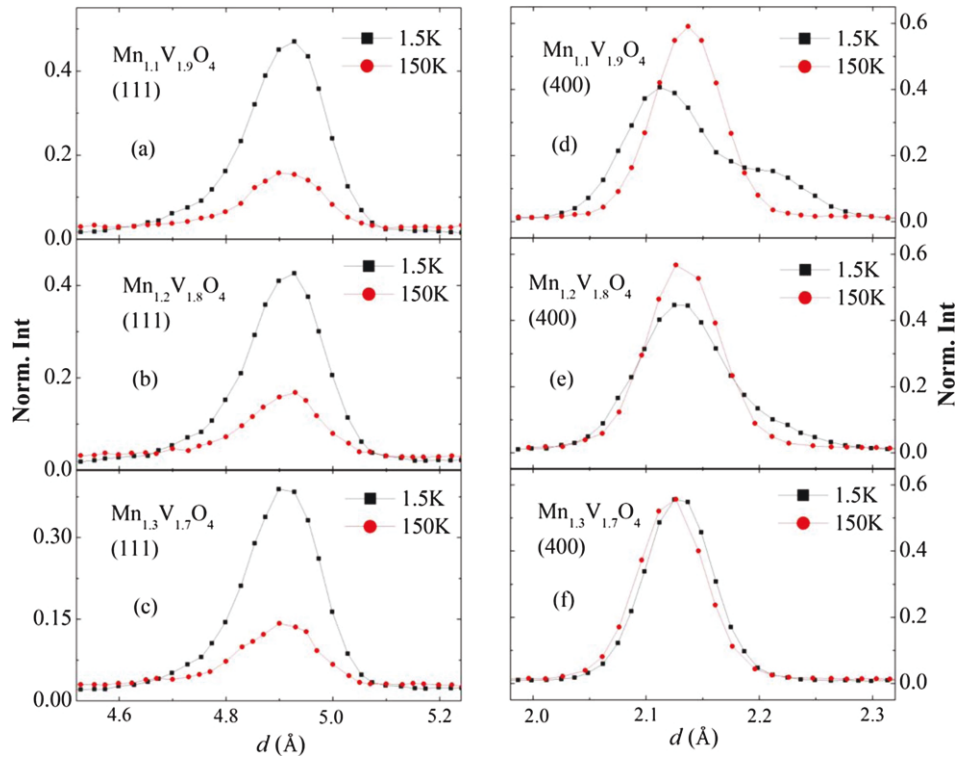

Figure 3. (a)−(f), the (111) and (400) Bragg diffraction of $x = 0.1, 0.2, 0.3$ at 1.5 K and 150 K by the neutron powder diffractometer, HB-2A, $\lambda = 1.5401$ Å. The diffraction splitting from cubic to tetragonal phase was clearly demonstrated as $x = 0.1$.

antiparallel to each other was obtained. Unlike $Mn_{1-x}Co_xV_2O_4$ [10, 19], the indicator of the CF-to-NCF transition—the (002) reflection—was not captured in $Mn_{1+x}V_{2-x}O_4$ at 20 K due to the weak intensity from the powder average effect and the strong absorption effect of vanadium [20]. Hence, two

V^{3+} spins models of being antiparallel to Mn^{2+} spins along c-axis and canting in the ab-plane were analyzed. Although both fitting parameters (χ^2) were close, the simulations on the (111) diffraction, the inset of figure 4(c), clearly demonstrated the better fittings for the model with the canted
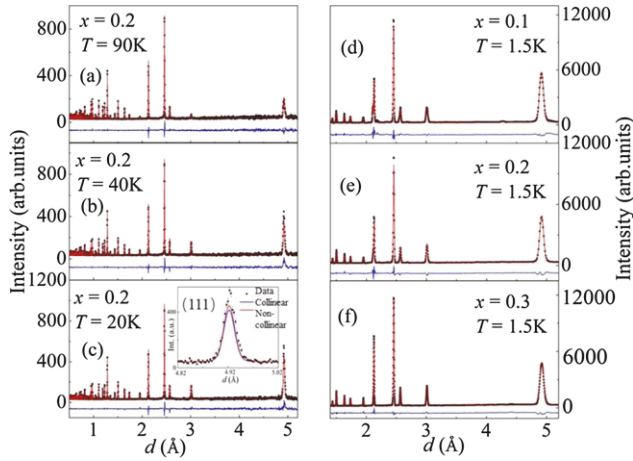
Figure 4. (a)–(c) Temperature-dependence of NPD data for $Mn_{1.2}V_{1.8}O_4$ by POWGEN, and (d)–(f) composition-dependence of NPD data for $Mn_{1+x}V_{2-x}O_4$ ($x = 0.1$, 0.2 and 0.3) with $\lambda = 2.41$ Å at 1.5 K by HB-2A, respectively. Black dots are the raw data, red lines are Rietveld refinements, and blue lines are the differences between observed and calculated intensities. Inset: fitting results of the (111) peak by different models.
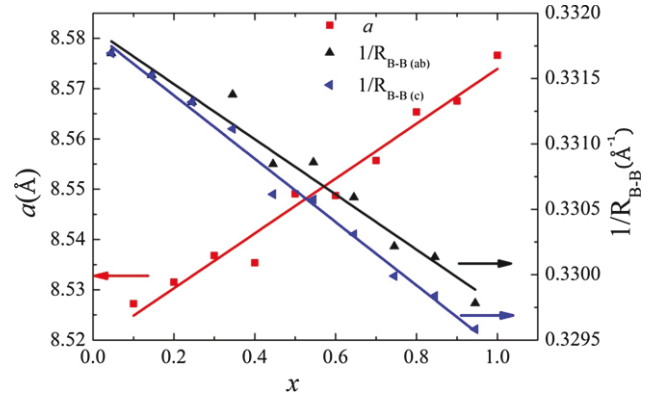

Figure 5. The composition-dependence of the lattice parameter a and the related $1/R_{B-B}$ along different directions for $Mn_{1+x}V_{2-x}O_4$ ($0.1 \leqslant x \leqslant 1$) at room temperature.

V^{3+} spins. Meanwhile, the A-site Mn^{2+} spins kept along the c-axis and B-site Mn^{3+} spins were still disordered. Actually, the models of the collinear/noncollinear Mn^{3+} spins were tested to identify the Mn^{3+} ordering with the high-resolution data at 1.5 K. For the collinear model, the NPD data could not be fitted very well with a ferromagnetism model using of Mn^{2+}– Mn^{3+} and a large Mn^{3+} moment. The model of noncollinear Mn^{3+} spins was not suitable, either. Therefore, the model of spins of V^{3+} canted from c-axis with the disordered Mn^{3+} spins was applied to refine the HB-2A data, figures 4(d)–(f). The canting angles of the V^{3+} spins decreased with increasing x ($x = 0.1$, 43.47°; $x = 0.2$, 35.75°; $x = 0.3$, 32.21°) which agreed with the $Mn_{1+x}Co_xV_2O_4$ results [10] and a smaller V^{3+}–V^{3+} bond length was recommended to MnV_2O_4.

Previously, both MnV_2O_4 and Mn_3O_4 have been confirmed as a normal spinel with Mn^{2+} ions at A-sites and V^{3+}/Mn^{3+} ions at B-sites [28, 29], while the Fe_2VO_4, Co_2VO_4 and Mg_2VO_4 were classified as inverse spinels [30–32]. Since Mn-doping affects both orbital effects and the valences of the Mn and V ions in $Mn_{1+x}V_{2-x}O_4$, two models of normal spinel and inverse spinel lattices were applied to refine the XRD and NPDs. The fitting result of $Mn_{1+x}V_{2-x}O_4$ was consistent with the normal spinel lattice for $x \leqslant 0.9$ for the XRD results, while there was no significant difference of χ^2 using normal or inverse spinel models for Mn_2VO_4. Therefore, the first-principle theory was performed on Mn_2VO_4 to analyze the accurate distribution of ions with the tetragonal lattice and will be discussed later. From the first-principle calculation, the average atomic potential energy of an inverse spinel is -7.98939 eV, while the normal spinel had the energy of -8.00222 eV or 12.8 meV lower. Therefore, Mn_2VO_4 was identified as a normal spinel with the tetragonal lattice.

In $Mn_{1-x}Co_xV_2O_4$ [20, 33], the smaller Co^{2+} ions not only increase chemical pressure in the system, but also shorten

the Co–Co, V–V and Co–V bond lengths. As $R_{V\text{-}V}$ is an indicator of the itinerant electron to weaken the orbital effect of V^{3+} ions at the B-site, the composition-dependence of the lattice constant and $1/R_{B-B}$ are shown to determine the orbital effects of V^{3+} ions and Mn^{3+} ions with Mn^{3+}-doping as shown in figure 5. The parameters for $x \geqslant 0.4$ are transferred from tetragonal to cubic lattice by multiplying a with $\sqrt{2}$: both lattice parameter and B–B bond length increase linearly with x. The increasing distance will reduce the chemical pressure and structural isotropy, which is contrary to the properties of $Mn_{1-x}Co_xV_2O_4$. Thus, the doped Mn^{3+} ions localize the electrons and reduce T_1 by weakening the superexchanges of J_{AB} and J_{BB}.

3.2. Magnetization and heat capacity

The temperature-dependent zero-field-cooled (ZFC) and field-cooled (FC) magnetizations of $Mn_{1+x}V_{2-x}O_4$ ($0.1 \leqslant x \leqslant 1$) under a 100 Oe magnetic field were shown in figure 6. As temperature decreased, a clear rise was observed at T_1, which corroborated the magnetic phase transition from PM to CF order [18, 28]. We also measured the temperature dependence of the specific heat (C_P–T curve) in zero magnetic field for all the samples, and one peak was observed in each C_P–T curve at the same temperature, T_1. Based on the diffraction measurements, the peak shape broadens as the Mn^{3+} content increases. For samples with $x \leqslant 0.3$, we observed a sharp peak which should correspond to the structural and magnetic transition simultaneously occurring at T_1 and T_S. For samples with $0.4 \leqslant x \leqslant 1$, the broad peak only corresponds to the magnetic order transition. The inset of figure 8 demonstrates the weak and broad anomaly on the H_C–T curve of $Mn_{1.8}V_{1.2}O_9$, similar as $Mn_{1.9}V_{1.1}O_4$. An extra anomaly could be observed at lower temperatures in the high doping ($x \geqslant 0.4$) ZFC curve. In order to probe the magnetic phase transition of $Mn_{1+x}V_{2-x}O_4$ ($0.1 \leqslant x \leqslant 1$) in detail, the derivative of the ZFC magnetization was shown in figure 7. Besides T_1, another peak marked as T_2 was observed in each curve below the T_1. As MnV_2O_4 [19], T_2 should correspond to the spin canting transition of V^{3+}. Both T_1 and T_2 decreased with Mn^{3+}-doping. Since the magnetic transition from CF-to-NCF was expected to relate the orbital
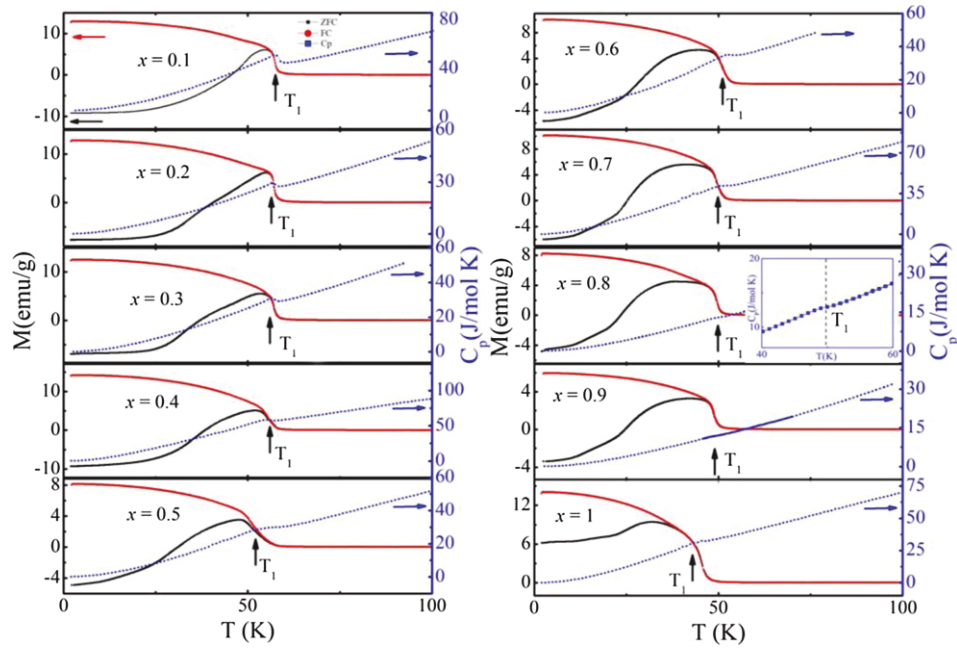
Figure 6. The temperature dependence of magnetization and specific heat for $Mn_{1+x}V_{2-x}O_4$ ($0.1 \leqslant x \leqslant 1$). Black and red lines are the results of the ZFC and FC measurements, respectively. The blue line represents the specific heat data. T_1, which corresponds to the PM to CF transition temperature, is obtained from both magnetization and specific heat. Inset: the enlarged H_C-T data around T_1 of $x = 0.8$.
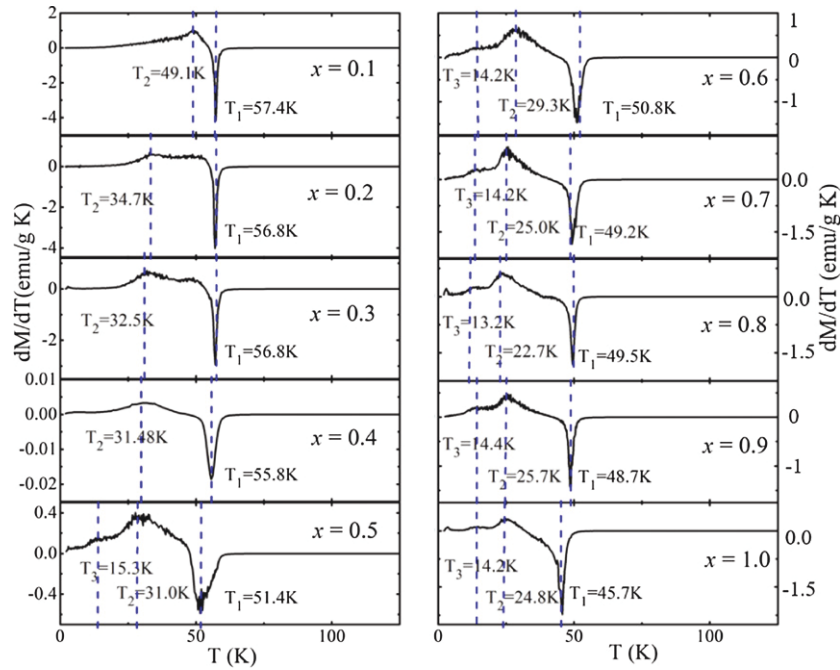

Figure 7. The first derivative ZFC curve of $Mn_{1+x}V_{2-x}O_4$ ($0.1 \leqslant x \leqslant 1$). T_1 represents the transition temperature of PM to CF, T_2 corresponds to the transition temperature from CF to the NCF1, and T_3 is the temperature from the first non-collinear ferrimagnetism to the NCF2.

ordering of V^{3+} ions [19], the sharp decreasing T_2 suggested the dilute effect from the Mn^{3+} ions. For $x \geqslant 0.5$, the third signal was observed, which should be the collinear to non-collinear transition of the Mn^{3+} ions [21, 25, 26, 33]. Actually, both the noncollinear phase transition of T_2 and T_3 were associated with competition between J_{AB} and J_{BB} and spin–orbit coupling of magnetic Mn^{3+} and V^{3+} ions at B-sites. We will discuss the mechanism for these transitions later.

3.3. First principles calculation

In order to study the orbital effects on the related superexchange, the partial density-of-states (DOS) of Mn_2VO_4 were calculated with the normal spinel and inverse spinel lattices, respectively (figure 8). First-principle calculations of the electronic structures for normal spinel and inverse spinel Mn_2VO_4 were carried out with the Vienna ab initio simulation package [34]. The projector augmented-wave method within the
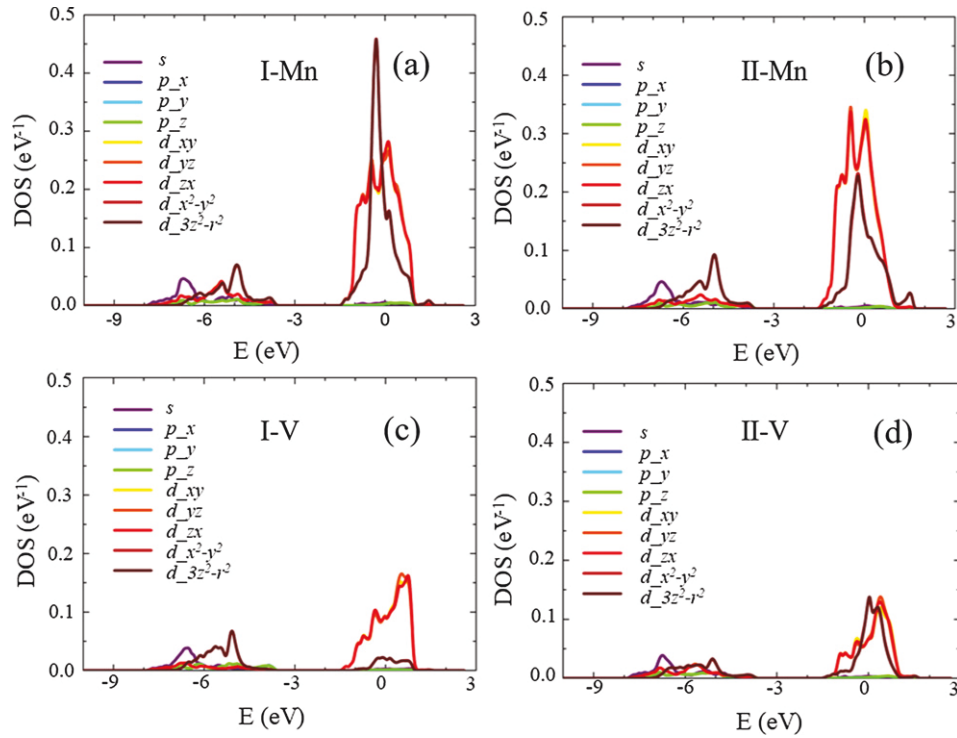
Figure 8. DOS of Mn_2VO_4 from DFT calculations. (a) and (b), DOS of Mn calculated by the normal spinel model (I) and inverse spinel model (II), respectively. (c) and (d), DOS of V calculated by the normal spinel model (I) and inverse spinel model (II), respectively.

density-functional theory was used to describe the interactions between ions and electrons [35], and the potential energy was determined without using any empirical input. Specifically, Perdew-Burke-Ernzerhof [36] functional under the general gradient approximation and a plane-wave cutoff of 400 eV were used. To accurately describe the atomic structure of AB_2O_4 with chemical occupation disorder, a super cell containing 448 atoms (64 A^{2+}, 128 B^{3+}, 256 O^{2-}) was adopted for both normal and inverse spinel lattices, with the occupation disorders being imitated via random number generation. For the spinel lattice, the 64 A^{2+} sites contain only Mn^{2+} ions, whereas the 128 B^{3+} sites are randomly filled with 64 Mn^{3+} and 64 V^{3+} ions. For the inverse spinel lattice, the 64 A^{2+} sites are randomly filled with 32 Mn^{2+} and 32 V^{2+} ions, whereas the 128 B^{3+} sites are randomly filled with 96 Mn^{3+} and 32 V^{3+} ions. For accurate electronic structure calculations, the Brillouin zone was sampled with a 3 × 3 × 3 k-point mesh. For comparison, the partial electronic density of states for different elements were normalized by the number of atoms for each element. Although the calculation was based on Mn_2VO_4, the DOSs of Mn^{3+}-/V^{3+}-ions in normal spinel and inverse spinel lattices were similar in the whole x range: i) The s- and p-orbital DOSs were similar for both normal spinel and inverse spinel; ii) the difference between normal spinel and inverse spinel of d-orbital DOSs was distinct. For normal spinel structure (I), the e_g ($3z^2−r^2$) DOS of Mn^{3+}-ion had a sharp peak around Fermi surface, while t_{2g} orbitals were dominant in inverse spinel (II). Unlike inverse spinel, the t_{2g} DOS of normal spinel V^{3+}-ion was larger than e_g orbitals. As expected, the result of normal spinel structure was consistent with the orbital ordering in previous studies [17, 23].
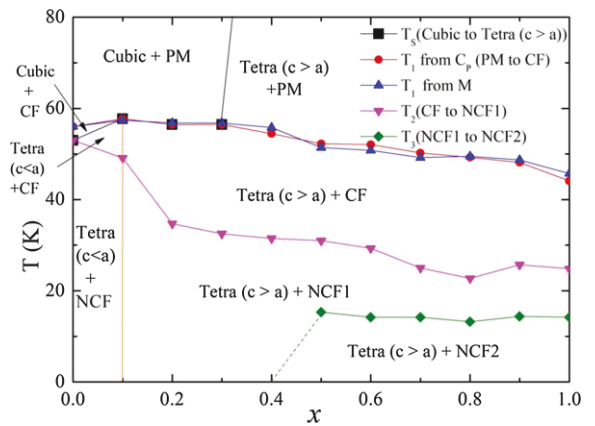

Figure 9. The temperature versus Mn^{3+} content (x) phase diagram of $Mn_{1+x}V_{2-x}O_4$. T_S is the cubic-to-tetragonal lattice transition temperature (black lines and squares) obtained from XRD. T_1 is the paramagnetic-to-collinear ferrimagnetic phase transition temperature (red line/dots and bule line/triangles) obtained from heat capacity and magnetization measurements, respectively. T_2 is the CF–NCF1 phase transition temperature (pink line/triangles) from magnetization measurement, where the spins of V^{3+} ions cant in the ab-plane with that of the Mn^{3+} ions align along the c-axis. T_3 is the temperature from NCF1 to NCF2 (olive line/rhombuses), and the spins of Mn^{3+} ions cant in ab-plane. The MnV_2O_4 data are from reference [29].

3.4. Phase diagram

Combining the heat capacity, magnetization, XRD and neutron diffraction data, the temperature (T) vs composition (x) phase diagram of $Mn_{1+x}V_{2-x}O_4$ was constructed in figure 9. This

complicated phase diagram clearly presents Mn^{3+}-doping effects on the JT distortion, the spin–orbit coupling, the competition of exchange interactions among different sites and the chemical pressure in the system. T_S corresponds to the structural phase transition from a cubic to a tetragonal phase, which was obtained from heat capacity and XRD measurements. T_1 represents the magnetic phase transition temperature from PM to CF. T_2 and T_3 are the CF–NCF1 and first non-collinear ferrimagnetism (NCF1)–second noncollinear ferrimagnetism (NCF2) phase transition temperatures, where the spins of V^{3+} and Mn^{3+} ions cant from the c-axis in the ab-plane, respectively.

4. Discussions

Although the tetragonal phase, $I4_1/amd$, is observed in the whole Mn^{3+}-doped MnV_2O_4 system, the low-doping compounds ($0 \leqslant x \leqslant 0.1$) have $c/a < 1$, similar to MnV_2O_4, while the high-doping compounds ($x > 0.1$) have $c/a > 1$, similar to Mn_3O_4. Moreover, T_S is not observed up to 300 K above $x = 0.3$ and should be determined by the collaboration of the orbital effects of the Mn^{3+} and V^{3+} ions.

The structural phase transition in MnV_2O_4 was associated with the orbital ordering of V^{3+} ions on the B-sites [18, 19, 37, 38]. Since the d orbitals of the V^{3+} ions split into three low-energy t_{2g} orbitals and two high-energy e_g orbitals, two outer shell electrons of the V^{3+} ion localized on the threefold-degenerate t_{2g} orbital. One electron occupied the xy orbital, and the other had the freedom of filling the yz or zx orbital or both of them with partial probabilities along the c-axis [17], which agreed with the dominant contribution from the t_{2g} orbitals of V^{3+} DOS as shown in figure 8(c). Hence, the shielding effect of electrons on the central ion was weak along the c-axis, and the central nucleus could suffer an attractive force from the c-direction which distorted the V^{3+}-lattice along the c-axis. The JT effect was not only confined at the V-pyrochlore, but also interfered with the whole crystal to drive the structural transition from a cubic to a tetragonal ($c < a$) phase.

On the other hand, the Mn^{3+} ($3d^4$) ions located at the center of a tetragonal MnO_4 with high spin configuration and the only electron occupied the e_g $3z^2-r^2$ orbit. Just as the dominated contribution of $d(3z^2-r^2)$ in Mn^{3+} DOS around the Fermi surface in figure 8(a). The similar tetragonal phase ($c > a$) was observed in Mn_3O_4, and the transition of cubic to tetragonal occurred at 1443 K [39]. Therefore, the structural phase of $Mn_{1+x}V_{2-x}O_4$ for low Mn^{3+}-doping ($x \leqslant 0.3$) at T_S could be regarded as the result of orbital ordering competition between Mn^{3+} and V^{3+} with the compression and elongation of BO_6 octahedron, respectively. Compared with the diagonal orbitals of the V^{3+} ions, the Mn^{3+} ions occupied the orbital along the axis and influenced the crystal distortion more easily. As a consequence, the $c/a > 1$ tetragonal phase appeared at T_S. For high Mn^{3+}-doping ($x \geqslant 0.4$), the lattice kept a tetragonal phase up to room temperature, indicating that the orbital ordering of Mn^{3+} ions suppressed the V^{3+} orbital completely.

Furthermore, the magnetic phase transition temperatures were strongly related to the Hamiltonian of the exchange energy. The full magnetic Hamiltonian might include the

isotropic Heisenberg exchange constants and the anisotropies:

$$
H = J_{AB} \sum_{(p,q)(i,j,k,l)} (S_p + S_q) \cdot (S_i + S_j + S_k + S_l)
$$
$$
+ J_{BB}^{ab} \left(\sum_{i,j} S_i \cdot S_j + \sum_{k,l} S_k \cdot S_l \right)
$$
$$
+ J_{BB}^c \sum_{(i,j)(k,l)} (S_i + S_j) \cdot (S_k + S_l)
$$
$$
+ D_A \sum_{r=p,q} (\hat{z} \cdot S_r)^2 + D_B \sum_{s=i,j,k,l} (\hat{u}_s \cdot S_s)^2, \quad (2)
$$

where J_{AB}, J_{BB}^{ab}, and J_{BB}^c were nearest-neighbor interactions. The inequivalent A-sites were given by subscripts p and q, and the inequivalent B-sites were given by subscripts i, j, k and l. D_A and D_B were along the c-axis and $\langle 111 \rangle$ direction, respectively.

At T_1, the spins of Mn^{2+} and V^{3+} aligned antiparallel to each other and formed a collinear magnetic ordering phase, while the spins of Mn^{3+} at B-sites still kept a disordered state. Since the antiferromagnetic exchange energy of Mn^{3+}–Mn^{3+}(J_{BB}^{ab}) was much stronger than the Mn^{3+}–Mn^{2+} coupling (J_{AB}), a collinear magnetic structure could not form under frustration. There were two paths to achieve magnetic interactions between nearest-neighbor Mn^{3+} ions [40, 41], the direct exchange interactions between the neighboring t_{2g} orbitals which were antiferromagnetic, and the superexchange interaction involving neighboring e_g electrons and middle oxygen's $2p$ orbital which was ferromagnetic. Therefore, the exchange interaction of Mn^{3+}–Mn^{3+} exhibited antiferromagnetically in the ab-plane, and J_{BB}^c was weak along the c-axis due to elongation of BO_6 octahedra. With the strong competition of J_{AB} and J_{BB}, a collinear Néel phase could not appear in Mn_3O_4 whereas a noncollinear ferrimagnetic YK phase presented instead [21, 41]. However, J_{BB} was not strong compared with J_{AB} in MnV_2O_4 and the V^{3+} spins aligned parallel to each other to produce collinear long-range ordering. Therefore, the Mn^{3+} spins remained disordered but the V^{3+} spins ordered at T_1 in $Mn_{1+x}V_{2-x}O_4$ ($x \leqslant 0.3$). With more Mn^{3+}-doping, the total exchange energy would decrease by reducing the first part of Hamiltonian mainly. Thus, the long-range spin order could be disturbed by thermal perturbation and T_1 decreased with increasing x.

Next, T_2 and T_3 in figure 9 were derived from the canting spins on B-sites of the Mn^{3+} ions and V^{3+} ions, respectively. The first NCF phase (NCF1) was from the canting V^{3+} spins and the second NCF phase (NCF2) was from that of the Mn^{3+} spins. The similar noncollinear magnetic phase transitions are both found in MnV_2O_4 [19] and Mn_3O_4 [42]. In both NCF phases, the Mn^{2+} spins aligned along the c-axis, while the B^{3+} spins had a c-axis component, which were antiparallel to the Mn^{2+} spins. The whole exchange energy on B-sites would lower the full spin Hamiltonian of spinels, and the absolute value of the spin Hamiltonian decreased by substituting a V^{3+} ion with a Mn^{3+} ion. Because the J_{BB}^{ab} of the Mn^{3+} ion was two times larger than that of the V^{3+} ion [40], the transition temperature T_2 from CF to NCF of V^{3+}

occurred at higher temperature and the NCF of Mn^{3+} at a lower temperature T_3. Just as illustrated before, the second NCF phase was not captured by magnetization for the $x \leqslant 0.4$ region due to the less amount of enough Mn^{3+}. For the high-doping region ($x \geqslant 0.5$), although T_3 occurs, it did not change significantly as x changed.

5. Conclusion

In summary, the orbital effects of the Mn^{3+} and V^{3+} ions in $Mn_{1+x}V_{2-x}O_4$ have been studied, and a phase diagram of composition versus temperature was constructed: (1) $0.0 \leqslant x < 0.1$, the cubic to tetragonal ($c/a < 1$) phase transition was observed as MnV_2O_4; (2) $0.1 \leqslant x \leqslant 0.3$, the system showed a tetragonal phase with $c/a > 1$ below T_S due to the orbital ordering of Mn^{3+}; (3) $x \geqslant 0.4$, the crystal structure keeps the tetragonal phase up to room temperature. Due to the competition of J_{AB} and J_{BB}, both T_1 and T_2 decreased with the increasing Mn-content, and the canting angle of $V^{3+}-V^{3+}$ decreased with large exchange energy on B sites. Moreover, a Mn^{3+} ions noncollinear magnetic ordering phase was observed at about 15 K for $x \geqslant 0.5$. As $Mn_{1-x}Co_xV_2O_4$ [20] and $Fe_{1-x}Co_xV_2O_4$ [43], the decoupling of lattice and magnetic transitions in $Mn_{1+x}V_{2-x}O_4$ can be explained by the induced competition between the orbital ordering and electronic itinerancy.

Data availability statement

All data that support the findings of this study are included within the article (and any supplementary files).

Acknowledgments

ORCID iDs

J L Jiao ⓘ https://orcid.org/0000-0002-5896-3729
J Ma ⓘ https://orcid.org/0000-0002-7060-1325

References

[1] Balents L 2010 *Nature* **464** 199
[2] Bramwell S T and Gingras M J P 2001 *Science* **294** 1495
[3] Zhou Y, Kanoda K and Ng T-K 2017 *Rev. Mod. Phys.* **89** 025003
[4] Ma J *et al* 2016 *Phys. Rev. Lett.* **116** 087201
[5] Jackeli G and Khaliullin G 2009 *Phys. Rev. Lett.* **102** 017205
[6] Oleś A M 2012 *J. Phys.: Condens. Matter.* **24** 313201
[7] Kiswandhi A, Ma J, Brooks J S and Zhou H D 2014 *Phys. Rev. B* **90** 155132
[8] Lee J H *et al* 2017 *Sci. Rep.* **7** 17129
[9] Lin G T *et al* 2018 *Phys. Rev. B* **97** 064405
[10] Ma J *et al* 2014 *Phys. Rev. B* **89** 134106
[11] Hu S-j, Yan S-s, Zhang Y-p, Zhao M-w, Kang S-s and Mei L-m 2014 *J. Appl. Phys.* **116** 043711
[12] Khomskii D 2009 *Physics* **2** 20
[13] Jahn H A 1938 *Proc. R. Soc. A* **164** 117
[14] Kugel K I and Khomskii D I 1973 *Sov. Phys. JETP* **37** 1429
[15] Khomskii D I and Mizokawa T 2005 *Phys. Rev. Lett.* **94** 156402
[16] Tchernyshyov O 2004 *Phys. Rev. Lett.* **93** 157206
[17] Tsunetsugu H and Motome Y 2003 *Phys. Rev. B* **68** 060405
[18] Suzuki T, Katsumura M, Taniguchi K, Arima T and Katsufuji T 2007 *Phys. Rev. Lett.* **98** 127203
[19] Garlea V O, Jin R, Mandrus D, Roessli B, Huang Q, Miller M, Schultz A J and Nagler S E 2008 *Phys. Rev. Lett.* **100** 066404
[20] Ma J *et al* 2015 *Phys. Rev. B* **91** 020407
[21] Suzuki T and Katsufuji T 2008 *Phys. Rev. B* **77** 220402
[22] Murakami Y *et al* 1998 *Phys. Rev. Lett.* **81** 582
[23] Nii Y, Sagayama H, Umetsu H, Abe N, Taniguchi K and Arima T 2013 *Phys. Rev. B* **87** 195115
[24] Huq A *et al* 2019 *J. Appl. Crystallogr.* **52** 1189
[25] Rodríguez-Carvajal J 1993 *Physica* B **192** 55
[26] Chung J-H, Hwan Lee K, Song Y-S, Suzuki T and Katsufuji T 2013 *J. Phys. Soc. Japan* **82** 034707
[27] Guillou F, Thota S, Prellier W, Kumar J and Hardy V 2011 *Phys. Rev. B* **83** 094423
[28] Kemei M C, Harada J K, Seshadri R and Suchomel M R 2014 *Phys. Rev. B* **90** 064418
[29] Zhou H D, Lu J and Wiebe C R 2007 *Phys. Rev. B* **76** 174403
[30] Bosi F, Skogby H, Fregola R A and Hålenius U 2016 *Am. Mineral.* **101** 580
[31] Mu C *et al* 2020 *Adv. Mater.* **32** 1907168
[32] Abe M, Kawachi M and Nomura S 1974 *J. Solid State Chem.* **10** 351
[33] Kiswandhi A, Brooks J S, Lu J, Whalen J, Siegrist T and Zhou H D 2011 *Phys. Rev. B* **84** 205138
[34] Kresse G and Furthmüller J 1996 *Phys. Rev. B* **54** 11169
[35] Blöchl P E 1994 *Phys. Rev. B* **50** 17953
[36] Perdew J P, Burke K and Ernzerhof M 1996 *Phys. Rev. Lett.* **77** 3865
[37] Adachi K, Suzuki T, Kato K, Osaka K, Takata M and Katsufuji T 2005 *Phys. Rev. Lett.* **95** 197202
[38] Hardy V, Bréard Y and Martin C 2008 *Phys. Rev. B* **78** 024406
[39] van Hook H J and Keith M L 1958 *Am. Mineral.* **43** 69
[40] Chung J H, Kim J H, Lee S H, Sato T J, Suzuki T, Katsumura M and Katsufuji T 2008 *Phys. Rev. B* **77** 054412
[41] Pal S and Lal S 2017 *Phys. Rev. B* **96** 075139
[42] Kim M, Chen X M, Joe Y I, Fradkin E, Abbamonte P and Cooper S L 2010 *Phys. Rev. Lett.* **104** 136402
[43] Sinclair R, Ma J, Cao H B, Hong T, Matsuda M, Dun Z L and Zhou H D 2015 *Phys. Rev. B* **92** 134410